Electrochemiluminescence resonance energy transfer biosensing platform between g-C$_3$N$_4$ nanosheet and Ru–SiO$_2$@FA for dual-wavelength ratiometric detection of SARS-CoV-2 RdRp gene

Tengyue Yin, Yuhang Ye, Wenshuai Dong, Guifen Jie [*]

Key Laboratory of Optic-electric Sensing and Analytical Chemistry for Life Science, MOE, College of Chemistry and Molecular Engineering. Qingdao University of Science and Technology, Qingdao, 266042, PR China

ARTICLE INFO

ABSTRACT

Rational detection of syndrome coronavirus 2 (SARS-CoV-2) is crucial to prevention, control, and treatment of disease. Herein, a dual-wavelength ratiometric electrochemiluminescence (ECL) biosensor based on resonance energy transfer (RET) between g-C$_3$N$_4$ nanosheets and Ru–SiO$_2$@folic acid (FA) nanomaterials was designed to realize ultrasensitive detection of SARS-CoV-2 virus (RdRp gene). Firstly, the unique g-C$_3$N$_4$ nanosheets displayed very intense and stable ECL at 460 nm, then the triple helix DNA was stably and vertically bound to g-C$_3$N$_4$ on electrode by high binding affinity between ssDNA and g-C$_3$N$_4$. Meanwhile, trace amounts of target genes were converted to a large number of output by three-dimensional (3D) DNA walker multiple amplification, and the output bridged a multifunctional probe Ru–SiO$_2$@FA to electrode. Ru–SiO$_2$@FA not only showed high ECL at 620 nm, but also effectively quenched g-C$_3$N$_4$ ECL. As a result, ECL decreased at 460 nm and increased at 620 nm, which was used to design a rational ECL biosensor for detection of SARS gene. The results show that the biosensor has excellent detection sensitivity for RdRp gene with a dynamic detection range of 1 fM to 10 nM and a limit of detection (LOD) of 0.18 fM. The dual-wavelength ratio ECL biosensor has inestimable value and application prospects in the fields of biosensing and clinical diagnosis.

1. Introduction

At the end of 2019, COVID-19 pneumonia caused by the SARS-CoV-2 novel coronavirus first broke out, and spread around the world (aC. Liu et al., 2020). SARS-CoV-2 has a strong infecting ability, and spreads extremely fast, thus the number of infected people increases exponentially, which seriously threatens the survival and health of human beings (Shahdeo et al., 2022). Therefore, early detection and discovery of the SARS-CoV-2 virus are of great significance to human, and its early clinical diagnosis has become an extremely challenging task (Zhong et al., 2021). RdRp gene located in the ORF1ab region, it has remarkable specificity and detection accuracy, which can be distinguished from the SARS-CoV virus that is easily confused with it (Fan et al., 2021). In the United States and Europe, real-time reverse transcriptase-polymerase chain reaction (RT-PCR) targeting the RdRp gene has become the gold standard (Engelmann et al., 2021). However, RT-PCR detection has the disadvantages of high start-up capital, easy RNA degradation, and high requirements on the quality of operators (Shahdeo et al., 2022).

Therefore, it is essential to find an efficient, simple, fast, and accurate detection method.

Electrochemiluminescence is a new detection method that combines the advantages of chemiluminescence and electrochemistry (Ge et al., 2019). Compared with other detection methods, it has the advantages of low background signal, simple operation, controllable program, and fast detection speed (Muzyka et al., 2017; Pu et al., 2018; Zhu et al., 2017). ECL technology helps to achieve accurate and sensitive detection of the SARS-CoV-2 virus RdRp gene. Traditional ECL detection methods often detect the corresponding target according to a single transmitter and signal changes. However, due to the existence of environmental changes and other factors, the real signal value is often disturbed, resulting in the appearance of false-positive signals (Cheng et al., 2014; Wu et al., 2016).

In view of this, the ratio type ECL detection method came into being. It is usually divided into two detection modes: dual wavelength and dual potential (Liu et al., 2019; Zhu et al., 2020), both of which are based on the ratio of the signals from two emitters. The concentration of the object establishes a linear relationship, thereby eliminating the

interference of the external environment and achieving high-accuracy detection of target object (Gai et al., 2017; Ye et al., 2019). In general, dual-potential ECL detection faces two major challenges, the choice of shared co-reactants and the matching of two emitters located at different emission potentials, which limited its development. While dual-wavelength ECL detection technique is a collection of two wavelength-dependent emitters that correlate the luminescence intensities and achieve target assay by ECL-RET, which avoids the limitation of co-reactant sharing. Compared with the former, it has a brighter application prospect (Huang et al., 2016). In recent years, ECL-RET systems based on quantum dots, luminol, and $Ru(bpy)_3^{2+}$ have been reported continuously. Zhu et al. reported an ECL-RET system based on luminol and CdSe@ZnS quantum dots system to efficiently detect thrombin (Dong et al., 2016). Wei et al. also reported a $Ru(bpy)_3^{2+}$ ECL-RET platform for insulin assay (Ma et al., 2016).

With the continuous exploration of electrochemiluminescent substances, new ECL materials emerge, such as graphene oxide modified with copper oxide and gold nanoparticles (Sun et al., 2022; Agrawal et al., 2020), Zr-MOFs having excellent heat resistance (Ma et al., 2021) and biocompatible new carbon-based material g-C_3N_4 (Medetalibeyoğlu, 2021), their appearance promotes the vigorous development of ECL technology. Graphitic carbon nitride nanosheets (g-C_3N_4NSs), as an emerging two-dimensional non-metallic semiconductor material, have been widely used and even sparked a gold rush in optoelectronics, catalysis and optical sensing fields for good electrical conductivity, well biocompatibility, and large specific surface area (Ong et al., 2016; Volokh et al., 2019; Zhou et al., 2018). Furthermore, it was applied to construction of biosensors due to its excellent electrochemiluminescence properties (Majdoub et al., 2020; Medetalibeyoğlu, 2021; Chen et al., 2022). $Ru(bpy)_3^{2+}$ as a classic ECL emitter displayed unparalleled ECL efficiency. However, $Ru(bpy)_3^{2+}$ itself is more prone to dissolution and diffusion in the liquid system, so it is also criticized in terms of stability (Feng et al., 2016; Li et al., 2012). By coating Ru $(bpy)_3^{2+}$ in SiO_2 carrier, which can prevent the dissolution of $Ru(bpy)_3^{2+}$ in the surrounding environment, this is a near-perfect solution strategy. It solves the problems of signal loss and poor stability of $Ru(bpy)_3^{2+}$ itself. At the same time, relying on the easy surface modification of the SiO_2 carrier, it can be more flexibly applied to various ECL biosensors (Yang et al., 2022).

In recent years, to improve the assay performance of biosensors, researchers have been working on developing new ECL materials with good stability, high electrical conductivity, and prominent ECL signals (Guo et al., 2018; Maar et al., 2019; Wei et al., 2019). However, this exploration of ideal luminous material often face many challenges, so the biological amplification technology can become a potential alternative strategy. So far, traditional biological amplification methods are all effective means to improve the sensitivity of biosensors (Chang et al., 2016; Dai et al., 2018; Hyeon et al., 2018; Tang et al., 2017). However, some experiments with harsh reaction conditions and complicated operating procedures limit their applications (Qing et al., 2018). As an important DNA nanomachine, 3D DNA walker can move incrementally and autonomously, thereby achieving efficient amplification of targets (Wu et al., 2019). By breaking through the barrier of DNA walker on one foot, a bipedal 3D DNA walker with higher efficiency and high delivery capability of target was designed, which is different from immune recognition (Zhao et al., 2019), enzyme drive (Feng et al., 2018; Xu et al., 2019), and toes (Yang et al., 2018). The 3D DNA walker that mediates the control of the strand displacement reaction will have an immeasurable impact on improving the sensitivity of ECL sensors (Wu et al., 2019).

Inspired by the above study, the g-C_3N_4 nanosheets and Ru–SiO_2@FA were acted as both dual-wavelength ECL emitters and resonance energy transfer system, which was used to fabricate a unique ECL biosensor for detection of SARS-CoV-2 virus gene. Herein, the novel multi-functional Ru–SiO_2@FA complex was prepared by linking FA to the amino groups of Ru–SiO_2, in which the UV absorption peak of

Ru–SiO_2 perfectly overlapped with the ECL maximum emission wavelength of g-C_3N_4 NSs and FA also displayed quenching effect on ECL of g-C_3N_4. Thus g-C_3N_4NSs and Ru–SiO_2@FA can form ECL RET system. Notably, g-C_3N_4 nanosheets and Ru–SiO_2 showed intense ECL at 460 nm and 620 nm, thus this dual-wavelength ECL biosensor was designed. After a trace amount of target genes were converted into a large number of output DNA by 3D DNA walker amplifier, the triple helix DNA was stably linked to g-C_3N_4 nanosheets, then the Ru–SiO_2@FA probe was bridged to the upright DNA on g-C_3N_4 nanosheets via output DNA. Thereby, the ECL of g-C_3N_4 at 460 nm was quenched by both Ru–SiO_2 and FA, and ECL of Ru–SiO_2 at 620 nm increased, thus the ratio of the ECL intensity at 620 nm and 460 nm has a reasonable linear relationship with the concentration of target RdRp gene, which confirms the feasibility and excellence of ratiometric ECL detection for target RdRp gene. More importantly, the highly sensitive and precise analysis of the RdRp gene of the SARS-CoV-2 virus by the ECL-RET biosensor is also significant for various other clinical biological tests.

2. Experimental section

2.1. Synthesis of g-C_3N_4NSs

The g-C_3N_4NSs are synthesized by slightly modifying the published method (Scheme 1C) (Zou et al., 2021). In detail, 5 g of melamine was placed in an alumina crucible with a lid, then heated to 550 °C in a muffle furnace, and kept at this temperature for 4 h. The obtained pale yellow blocky solid was ground into powder for subsequent use.

To improve ECL and water-solubility of g-C_3N_4NSs, a liquid exfoliation method was used to modify the previously obtained bulk graphitic carbon nitride (Wang et al., 2019). Firstly, 1 mg of bulk graphitic carbon nitride was added to 100 mL of HNO_3 (5 M) and refluxed at 125 °C for 24 h, then the obtained product was centrifuged and finally dried in an oven at 60 °C overnight.

2.2. Synthesis of aminated SiO_2 microsphere

The aminated SiO_2 microspheres were synthesized refer to stÖber's method (Jie et al., 2019). Firstly, 12 mL of ethanol, 20 mL of ultrapure water, and 4 mL of $NH_3 \cdot H_2O$ were sequentially added to the three-necked flask, and the solution was stirred for 0.5 h under magnetic stirring to make it evenly mixed. Then 2 mL of tetraethoxysilane (TEOS) and 8 mL of ethanol solution were added to the above solution and stirred for 6 h. Next, 2 mL of APTES was added to continue stirring for more than 10 h. The product was centrifuged and washed with ethanol to obtain the aminated SiO_2 microspheres, then they were dissolved in 20 mL of ultrapure water for use.

2.3. Synthesis of Ru–SiO_2@FA

Specifically, the synthesis of Ru–SiO_2@FA was roughly divided into two steps. In the first step, Ru–SiO_2 nanosphere was prepared by a water-in-oil method according to previous literature (Xiong et al., 2019). $Ru(bpy)_3Cl_2 \bullet 6H_2O$ (340 μL, 0.1 M), TX-100 (1.7 mL), cyclohexane (7.5 mL), and n-hexanol (1.8 mL) were added to a clean three-necked flask, vigorously stirring in a water bath at 25 °C for 30 min, then a water-in-oil emulsion was obtained. After that, 100 μL of TEOS and 60 μL of $NH_3 \bullet H_2O$ were gradually added to react at room temperature for 24 h. Next, 10 mL of acetone was added to break the emulsion, after washing with ethanol and secondary water for multiple times, orange Ru–SiO_2 nanosphere was obtained. Afterward, 200 μL of APTES was added to the purified Ru–SiO_2 solution and stirred in a dark environment at 25 °C for 60 min. After that, the excess APTES on the surface was removed by multiple times of washing with ethanol and ultrapure water, thereby obtaining pure NH_2–Ru–SiO_2 nanosphere.

In the second step, 100 μL of EDC (0.1 M) and 100 μL of NHS (0.025 M) were added to 200 μL of 0.1 M FA solution, and the mixed solution
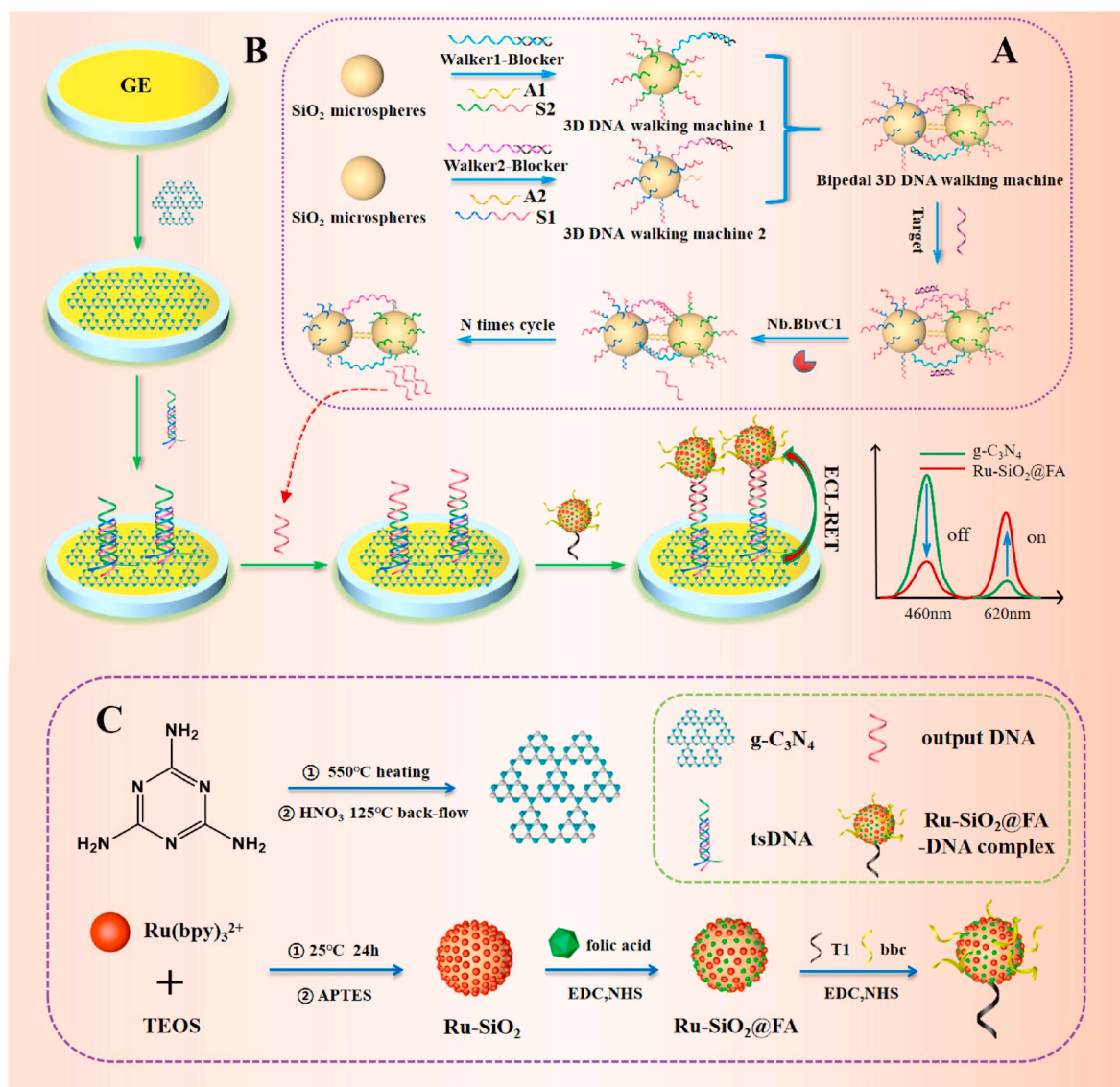
Scheme 1. Schematic illustration of a dual-wavelength ratiometric ECL biosensor based on RET platform of g-C$_3$N$_4$ nanosheets and Ru–SiO$_2$@FA for detection of SARS gene.

was incubated at 37 °C for 60 min. After centrifuging, the obtained solid was redispersed in 200 μL of ultrapure water. Next, it was mixed with an equal volume of NH$_2$–Ru–SiO$_2$ nanosphere obtained in the first step, incubated at 37 °C for at least 4 h, and centrifuged at 12,000 rpm, thus the final product Ru–SiO$_2$@FA was obtained.

2.4. Synthesis of Ru–SiO$_2$@FA-DNA bioconjugates

The preparation process of the Ru–SiO$_2$@FA-DNA probe is shown in detail in Scheme 1C. Firstly, 50 μL of 5 μM biocoding DNA (bbcDNA) was mixed with 50 μL of 1 μM probe DNA (T1), then 50 μL of 0.1 M EDC and 50 μL of 0.025 M NHS were added to them. The mixture was shaked and reacted at 37 °C for 40 min, then an appropriate amount of the purified Ru–SiO$_2$@FA was added to combine with them for 6 h. Finally, the free oligonucleotide was removed by centrifugation at 5000 rpm to obtain a pure Ru–SiO$_2$@FA-DNA bioconjugate probe.

2.5. Synthesis of triple helix DNA (tsDNA)

The ideal triple-helix DNA (tsDNA) structure is based on double-stranded DNA (dsDNA) and modified (bL. Liu et al., 2020). Briefly,

ssDNA-1 (100 μL, 10 μM) and ssDNA-2 (100 μL, 10 μM) were thoroughly mixed in TE buffer, then annealed at 95 °C for 5 min, and allowed to cool to room temperature naturally to obtain the dsDNA structure.

Next, 200 μL of ssDNA-3 (5 μM) and 200 μL of fresh MgCl$_2$ (Mg^{2+} concentration of 10 mM) were mixed with the above dsDNA solution and hybridized at 4 °C for more than 12 h to obtain the tsDNA structure.

2.6. The 3D DNA walker amplification process

Two independent walkers were combined to obtain the bipedal 3D DNA walker. First, 10 μL of 2 μmol/L blocker 1 was mixed with 10 μL of 2 μmol/L walker 1, and incubated at 37 °C for 2 h to prepare the walker 1-blocker 1. Correspondingly, the walker 2-blocker 2 was also made in the same way.

Next, 4 μL of walker 1-blocker 1 (1 μM), 80 μL of S2 (2 μM) and 2 μL of A1 (2 μM) with carboxyl groups were mixed with 50 μL of SiO$_2$ microsphere, incubated at 37 °C for more than 6 h, and centrifuged to remove any bound DNA, the obtained SiO$_2$-DNA precipitate was redissolved in 100 μL of water to obtain the 3D DNA walker 1, and the 3D DNA walker 2 was obtained in the same way. Finally, 100 μL of 3D DNA walkers 1 and 2 were mixed and incubated at 37 °C for 2 h, the 3D DNA

walkers 1 and 2 were connected through A1 and A2 to obtain the bipedal 3D DNA walker.

2 μL of Target DNA at different concentrations was added to 100 μL of the prepared bipedal 3D DNA walker solution and reacted at 37 °C for 2 h. The released walker 1 and walker 2 can hybridize with S1 and S2, respectively. Subsequently, 6 U of Nb.BbvCI endonuclease was added to the solution and reacted at 37 °C for 80 min. After cycling-digestion ampification process, a large amount of output DNA were obtained. After centrifugation, the supernatant containing the output DNA strand was stored at 4 °C for use.

2.7. Construction of the ECL biosensor

The electrode was firstly polished with Al_2O_3 powder, then cleaned with ultrapure water, and finally dried. After 10 μL of the previously prepared g-C_3N_4NSs (1 mg/mL) suspension was dropped on the electrode and air-dried naturally, 5 μL of tsDNA was added dropwise to the surface of g-C_3N_4NSs/gold electrode (GE) and incubated at 4 °C for 1.5 h to make the tsDNA stand upright on the surface of g-C_3N_4NSs. Similarly, 10 μL of the supernatant containing the output DNA strand and 10 μL of Ru–SiO_2@FA-DNA bioconjugate probe were sequentially dropped on the electrode surface and incubated. After each step of dropwise addition, the electrode surface needs to be rinsed to remove unbound product. The prepared ECL biosensor was stored at 4 °C for subsequent studies.

3. Results and discussion

3.1. Mechanism of the dual-wavelength ratiometric ECL biosensor for RdRp gene detection

The design principle of the dual-wavelength ratiometric ECL biosensor based on RET between g-C_3N_4 nanosheets and Ru–SiO_2@FA for assay of SARS-CoV-2 RdRp gene is shown in Scheme 1. Firstly, the bipedal 3D DNA walker amplification process was performed to greatly amplify RdRp gene concentration and improve detection sensitivity (Scheme 1A). The aminated SiO_2 microspheres with large surface area and uniform particle size were selected as carriers, and the walker was binded to SiO_2 via peptide bond. Target gene firstly competes to bind the blocker in walker-blocker duplex, releasing walker to bind the unpaired S-strand on the silica sphere. Then endonuclease recognized the walker-S duplex and cleaved the specific site to release the walker into the next cycle. As a result, a large number of output DNA were produced by multiple cycles of amplification. At the same time, the triple-helix DNA (tsDNA) with a highly rigid structure was formed by combining three specific ssDNA. Due to the high binding affinity of the ssDNA tail with graphitic carbon nitride and the poor affinity of triple-helical DNA with graphitic carbon nitride, the negatively charged tripod probe has a stronger repulsion, resulting in upright tripod structure on the g-C_3N_4NSs-modified electrode surface, thus the probe entanglement and potential steric hindrance of reactions can be effectively avoided. In addition, Ru–SiO_2@FA-DNA probe was formed by first linking FA to Ru–SiO_2 and followed connection of DNA to Ru–SiO_2@FA via peptide bond. Then output DNA bridged the Ru–SiO_2@FA-DNA probe to the
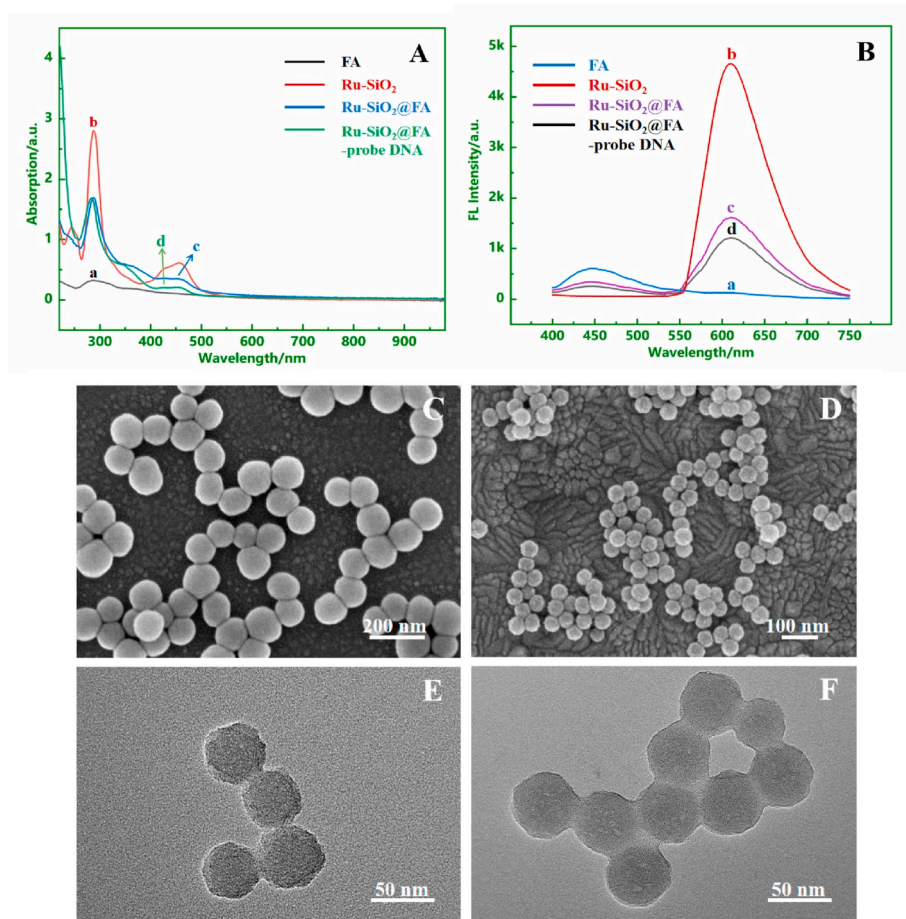

Fig. 1. (A) UV–Vis absorption spectra of (a) FA, (b) Ru–SiO_2, (c) Ru–SiO_2@FA, (d) Ru–SiO_2@FA-probe DNA. (B) Fluorescence spectra of (a) FA, (b) Ru–SiO_2, (c) Ru–SiO_2@FA, (d) Ru–SiO_2@FA-probe DNA. (C) SEM image of the aminated SiO_2 microsphere, (D) SEM image of Ru–SiO_2 microsphere, (E) TEM image of Ru–SiO_2 microsphere, (F) TEM image of Ru–SiO_2@FA-DNA probe.

triple-helical DNA on the electrode, ECL resonance energy transfer from g-C₃N₄ nanosheets to Ru–SiO₂@FA and FA quenching occurred, and the ratio value of the two ECL signals at 620 nm and 460 nm had a linear relationship with the amount of target, thus the dual-wavelength ratio ECL biosensor was developed for ultrasensitive detection of SARS gene.

3.2. Characterization of the SiO₂ microsphere, Ru–SiO₂ microsphere and Ru–SiO₂@FA-DNA probe

UV–Vis absorption spectroscopy (Fig. 1A) and fluorescence spectroscopy (Fig. 1B) were used to study the fabrication process of Ru–SiO₂@FA-DNA probe. From Fig. 1A, it can be found that the only absorption peak of FA located at 288 nm, while two absorption peaks of Ru–SiO₂ at 454 nm and 288 nm were observed. When FA was linked to Ru–SiO₂, the absorption peak of Ru–SiO₂@FA is the same as that of Ru–SiO₂, which is due to the overlapping of their absorption peaks at 288 nm. After further ligation with DNA, the UV–Vis absorption peak of Ru–SiO₂@FA-probe DNA shifted slightly from 288 nm to 280 nm, which also corresponded to the absorbance of oligonucleotide aptamers.

In Fig. 1B, Ru–SiO₂ only fluoresced at 610 nm, while FA only fluoresced at 450 nm. After the two were combined, the complex had fluorescence peaks at both 450 nm and 610 nm, so it can be proved that FA was successfully compounded on Ru–SiO₂. When DNA was attached, the fluorescence peak of the Ru–SiO₂@FA-DNA Probe did not change, while the signal became lower, perhaps the oligonucleotides affects the fluorescence.

Fig. 1C and D are SEM images of aminated SiO₂ microsphere and Ru–SiO₂ microsphere, respectively. It can be seen that the particle size of the two kinds of microspheres are uniform, among which the average diameter of the aminated SiO₂ microsphere is about 100 nm and the surface is relatively smooth, while the average diameter of the Ru–SiO₂ microsphere is about 40 nm, but the surface is relatively rough.

Fig. 1E and F are transmission electron microscopy (TEM) images of Ru–SiO₂ microsphere and Ru–SiO₂@FA-DNA probe, respectively. By comparison, an obvious cross-linked layer appears between the Ru–SiO₂@FA-DNA probe microspheres, they are the modified folic acid and probe DNA, and the surface becomes rough, which confirmed the successful preparation of Ru–SiO₂@FA-DNA probe.

Fig. 2 performed further elemental mapping analysis on the Ru–SiO₂@FA-DNA probe. As expected, the main elements observed were carbon, nitrogen, phosphorus, silicon, and ruthenium, corresponding to B to F in Fig. 2, respectively. Among them, silicon and ruthenium elements are mainly derived from Ru–SiO₂ microspheres, carbon and nitrogen elements are derived from FA and DNA probes, and phosphorus elements are derived from DNA probes alone. The results further confirmed that the assembly of the Ru–SiO₂@FA-DNA probe has been successfully completed.

3.3. Gel electrophoresis analysis of the bipedal DNA walker amplification, triple helix DNA synthesis and Ru–SiO₂@FA-DNA probe linking process

The feasibility of the bipedal DNA walker amplification, triple helix DNA synthesis and Ru–SiO₂@FA-DNA probe linking process were investigated by polyacrylamide gel electrophoresis (PAGE). Firstly, the chain replacement process is shown in Fig. 3A. Lane M is Marker, lanes 1 to 3 show Target DNA, Blocker DNA, and Walker DNA. When Blocker DNA was mixed with Walker DNA and Target DNA, respectively, two new higher bands were obtained (lanes 4 and 5), corresponding to the formed Walker-Blocker and Blocker-Target duplexes. When Target DNA was added to the Walker-Blocker hybrid strand, a new bright band of Blocker-Target DNA hybrid strand and free Walker were observed (lane 6), showing that Target DNA successfully competed with Blocker DNA to release Walker for achieving amplification.

As shown in Fig. 3B, lane M is Marker, lanes 1 to 4 show Walker DNA, S1 DNA, ssDNA-3, and T1 DNA. When Walker DNA was mixed with S1 DNA, a new higher band was obtained (lane 5), corresponding to the formed Walker-S1 duplex. After adding Nb.BbvCI endonuclease to the Walker-S1 hybrid strand, it was observed that the previous band corresponding to the Walker-S1 duplex disappeared, and a lower band appeared (lane 6), thus it was proved that Nb.BbvCI endonuclease successfully cut the double strand of Walker-S1 and obtained secondary target DNA S3. Next, after mixing the cleavage product S3 with ssDNA-3, T1, and ssDNA-3+T1 mixture, respectively, three new bright bands appeared correspondingly (lanes 7–9), suggesting S3 as a bridge can connect T1 in Ru–SiO₂@FA-DNA probe and ssDNA-3 on electrode. In addition, the two single-stranded A1 and A2 used to construct bipedal 3D DNA walkers are shown in lanes 1 and 2 of Fig. 3C, respectively. After hybridization, a band corresponding to the double-stranded A1-A2 appeared (lane 3), which verified the feasibility of bilateral hybridization and the construction of bipedal 3D DNA walkers.

The construction process of triple helix DNA is shown in Fig. 3C. Lane M is Marker and lanes 4 to 6 show ssDNA-1, ssDNA-2, and ssDNA-3. After ssDNA-1 was mixed with ssDNA-2, a new higher band was obtained (lane 7), corresponding to the formed ssDNA-1+ssDNA-2 duplex. When ssDNA-3 and MgCl₂ were added to the ssDNA-1+ssDNA-2 hybrid strand, a new higher band (lane 8) was observed, which proved the triple-helix DNA was constructed successfully.

3.4. Characterization of the biosensor construction process

SEM was used to characterize the morphology of g-C₃N₄NSs and the subsequent electrode construction process. Fig. S1A is SEM image of g-

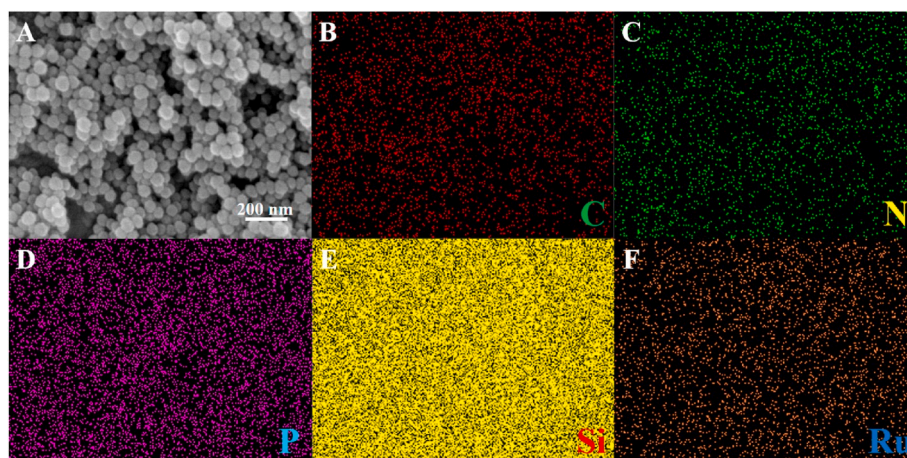**Fig. 2.** (A) SEM image of Ru–SiO₂@FA-DNA probe, SEM-EDX elemental mapping of (B) C, (C) N, (D), P, (E) Si and (F) Ru.
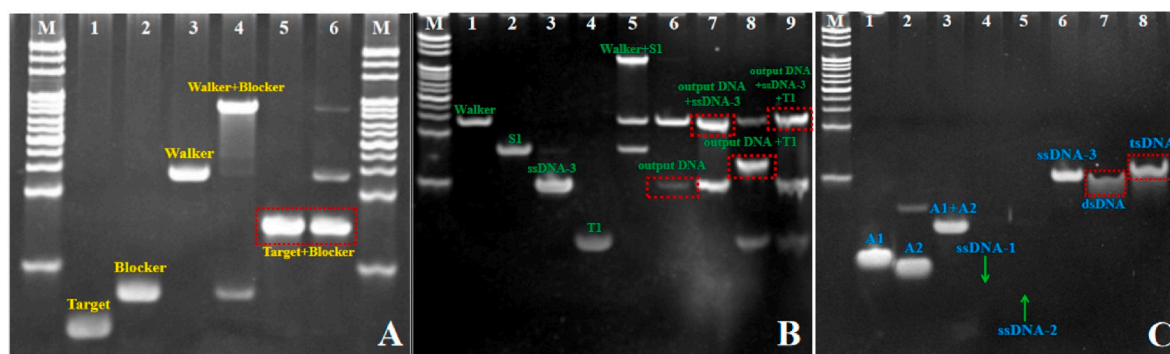
Fig. 3. (A) The strand displacement process for walker, Lane 1: Target DNA, Lane 2: Blocker DNA, Lane 3: Walker DNA, Lane 4: Walker + Blocker DNA, Lane 5: Target + Blocker DNA, Lane 6: Walker + Blocker DNA duplex + Target DNA, Lane M: Marker DNA. (B) The cycling amplification process, Lane 1: Walker DNA, Lane 2: S1 DNA, Lane 3: ssDNA-3, Lane 4: T1 DNA, Lane 5: Walker + S1, Lane 6: Walker + S1+Nb.BbvCI, Lane 7: Walker + S1+Nb.BbvCI + ssDNA-3, Lane 8: Walker + S1+Nb.BbvCI + T1, Lane 9: Walker + S1+Nb.BbvCI + ssDNA-3+T1, Lane M: Marker DNA. (C) The process for linking two SiO$_2$ microspheres of DNA walker and triple helix DNA construction, Lane 1: A1 DNA, Lane 2: A2 DNA, Lane 3: A1+A2; Lane 4: ssDNA-1, Lane 5: ssDNA-2, Lane 6: ssDNA-3, Lane 7: ssDNA-1+ssDNA-2, Lane 8: ssDNA-1+ssDNA-2 duplex + ssDNA-3+MgCl$_2$, Lane M: Marker DNA.

C$_3$N$_4$NSs. It can be seen that the prepared graphitic carbon nitride nanosheet has a uniform lamellar structure with an average size of about 2–3 μm and good dispersibility. Fig. S1B characterized the stages of sequential modification of g-C$_3$N$_4$NSs/tsDNA/Ru–SiO$_2$@FA-DNA probes on the surface of gold electrodes, it can be seen that many nanospheres were uniformly distributed on the flat surface of g-C$_3$N$_4$NSs, indicating that the biosensor has been successfully constructed.

3.5. Feasibility of the ECL biosensing platform for target detection

The feasibility of the dual-wavelength ratio ECL system was verified by comparative experiments. In Fig. 4A, the maximum ECL emission wavelength of g-C$_3$N$_4$NSs is located at 460 nm, while the maximum UV absorption wavelength of Ru–SiO$_2$ (excitation peak) is exactly at 455 nm, thus the perfect overlap of the two sides indicates that ECL-RET between Ru–SiO$_2$ and g-C$_3$N$_4$NSs can occur. In addition, the ECL signal changes of the electrode at 460 nm and 620 nm before and after adding output DNA were shown in Fig. 4B and C (curves b to c), and all the background signals can be ignored (curve a). The ECL signal at 460

nm is weakened after the addition of output DNA, this is due to the fact that Ru–SiO$_2$ is connected to the electrode and quenched ECL of g-C$_3$N$_4$NSs (Fig. 4B). Similarly, 620 nm is the optimal ECL emission peak of Ru–SiO$_2$ (Fig. 4C), and its signal value is significantly improved with the addition of output DNA. Interestingly, the introduction of FA further weakened the cathodic ECL signal of g-C$_3$N$_4$NSs, since FA competed for electrons to suppress the electronic transition between the conduction band and the valence band of g-C$_3$N$_4$NSs, reducing the generation of excited states of g-C$_3$N$_4$NSs (Zhou et al., 2016), the specific quenching mechanism is shown in Fig. S2. Fig. 4D shows the stability of ECL signals of the electrodes at 460 nm and 620 nm before and after the addition of output DNA. The ECL was scanned for 10 cycles in the range of 0 V to −1.5 V, few fluctuations were observed, indicating that the electro-chemiluminescence system has excellent stability. The results show that the ECL-RET between g-C$_3$N$_4$NSs and Ru–SiO$_2$ and the inhibition of electronic transitions between the conduction and valence bands of g-C$_3$N$_4$NSs by FA are effective, and the proposed ECL system is feasible. When the modified electrode was scanned from −1.5 V to 0 V, the g-C$_3$N$_4$NSs and the co-reactant K$_2$S$_2$O$_8$ on the electrode surface were
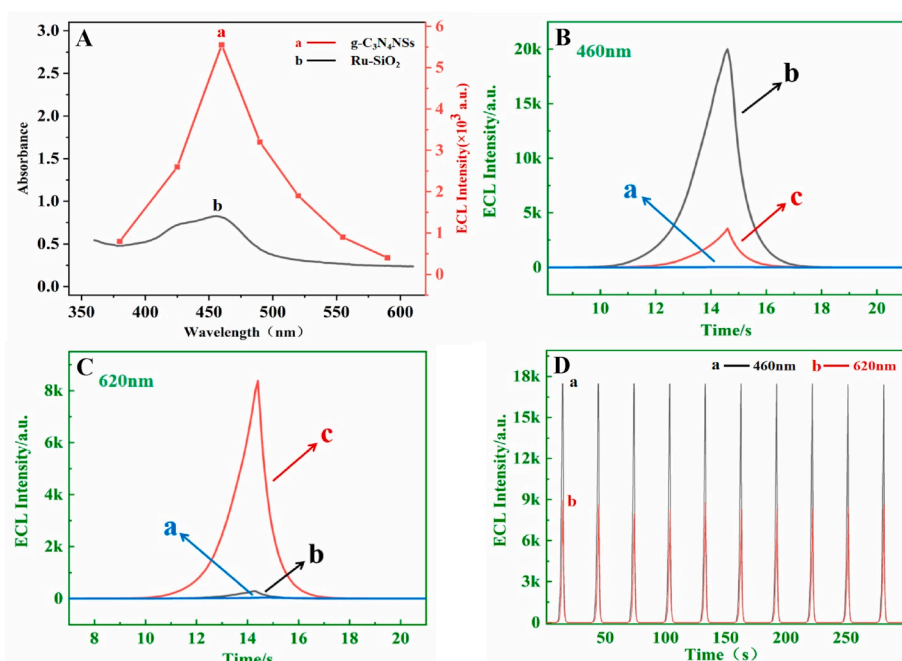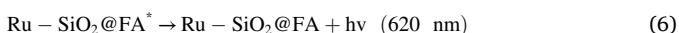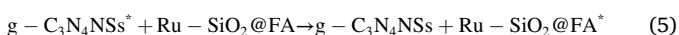

Fig. 4. (A) ECL spectrum of g-C$_3$N$_4$NSs (a, red line), UV–vis absorption spectrum of Ru–SiO$_2$ (b, black line). (B) ECL changes at the wavelength of 460 nm: (a) bare electrode, (b) before adding output DNA, (c) after adding output DNA. (C) ECL changes at the wavelength of 620 nm: (a) bare electrode, (b) before adding output DNA, (c) after adding output DNA. (D) ECL signal stability at 460 nm before adding output DNA (black line), ECL signal stability at 620 nm after addition of output DNA (red line).

simultaneously reduced to g-C₃N₄NSs$^{\bullet-}$ and SO₄$^{\bullet-}$, then they reacted to generate excited states g-C₃N₄NSs*. As the donor of the ECL-RET system, g-C₃N₄NSs* can transfer energy to Ru–SiO₂@FA to generate Ru–SiO₂@FA*, and finally Ru–SiO₂@FA* emitted light at 620 nm and returned to the ground state.

Therefore, the ECL signal of g-C₃N₄NSs was weakened, while the ECL response of Ru–SiO₂@FA increased. The quenching effect of Ru–SiO₂@FA on g-C₃N₄NSs cathode ECL can be attributed to ECL-RET and electron transfer. The ECL-RET process can be represented as follows (Liang et al., 2018):

$$g\text{-}C_3N_4NSs + e^- \rightarrow g\text{-}C_3N_4NSs^{\cdot-} \tag{1}$$

$$S_2O_8^{2-} + e^- \rightarrow SO_4^{2-} + SO_4^{\cdot-} \tag{2}$$

$$g\text{-}C_3N_4NSs^{\cdot-} + SO_4^{\cdot-} \rightarrow g\text{-}C_3N_4NSs^* + SO_4^{2-} \tag{3}$$

$$g-C_3N_4NSs^* \rightarrow g-C_3N_4NSs + h\nu \;\; (460 \;\; nm) \tag{4}$$

$$g-C_3N_4NSs^* + Ru-SiO_2@FA \rightarrow g-C_3N_4NSs + Ru-SiO_2@FA^* \tag{5}$$

$$Ru-SiO_2@FA^* \rightarrow Ru-SiO_2@FA + h\nu \;\; (620 \;\; nm) \tag{6}$$
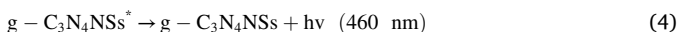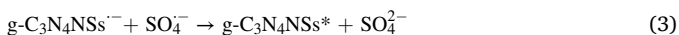
3.6. Optimization of experimental conditions

Experimental conditions for optimal ECL signal were optimized by detecting target concentration of 10 nM. The effect of Ru–SiO₂ microsphere solution with different dilution ratios (one-fold, two-fold, three-fold, four-fold, and five-fold, respectively) on ECL signal was studied. As shown in Fig. S3A, with the increase of the dilution ratio of Ru–SiO₂ solution, the change of ECL signal increased. When the dilution of Ru–SiO₂ solution reached 2 times, the change of ECL signal tended to be stable. Therefore, the Ru–SiO₂ microsphere solution was diluted 2-fold for the experiments.

SiO₂ microsphere was used as the carrier of DNA cyclic amplification, and the slight change of the concentration of SiO₂ microsphere solution has an important influence on the DNA cyclic amplification system and thus the ECL signal. As shown in Fig. S3B, as the concentration of SiO₂ solution decreases, the change value of the ECL signal increases. When the concentration of SiO₂ solution was diluted to 15 mg/mL, the change of the ECL signal tended to be stable. So the concentration was diluted to 15 mg/mL for experiments.

The dose of Nb.BbvCI endonuclease has a significant effect on the ECL signal change in the amplification process, the result is shown in Fig. S3C. With the increase of Nb.BbvCI endonuclease dosage, the ECL signal change value gradually increased, and became stable when the endonuclease dosage was 5 U. Therefore, 5 U of Nb.BbvCI was used in the experiments.

The digestion time has a significant impact on the yield of output DNA, thus the digestion time was optimized. Fig. S3D reflects that with the extension of the digestion time, the change value of the ECL signal increased significantly. When the time exceeded 120 min, the ECL signal change value no longer increased. Therefore, 120 min was chosen as the optimal digestion time for the detection system.

3.7. Analytical performance of the ratiometric biosensor

The ECL ratiometric biosensor based on RET of g-C₃N₄NSs and Ru–SiO₂ was constructed to detect target RdRp gene. Fig. 5A showed the ECL signal response of g-C₃N₄NSs at 460 nm with different concentrations of RdRp gene, and the ECL intensity gradually weakened with the increase of target gene concentration. Fig. 5B displays the signal responses of Ru–SiO₂ at 620 nm, and the ECL signal of Ru–SiO₂ gradually increased. Fig. 5C present good linear relationship between the ECL responses of g-C₃N₄NSs and Ru–SiO₂ with the concentrations of target gene. To obtain better accuracy and reliability of the ECL assay performance, the ratiometric method by ECL intensities of g-C₃N₄NSs and Ru–SiO₂ was employed to detect the target RdRp gene. In the concentration range of 10^{-6}–10 nM of target, the ECL ratio value was linearly dependent on the concentration of target RdRp gene (Fig. 5D). The
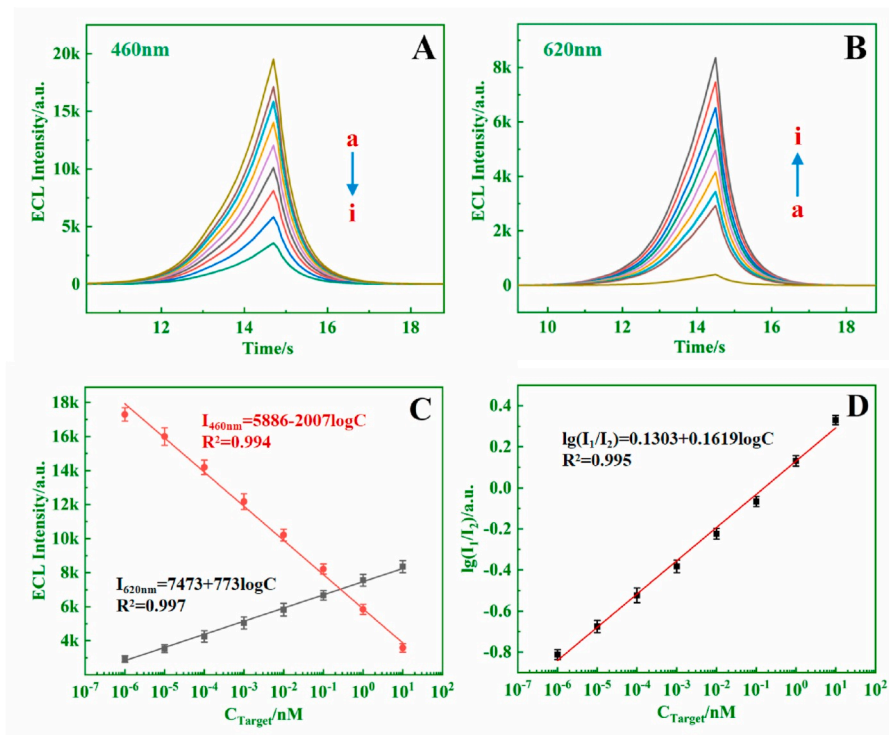

Fig. 5. ECL intensity-time curves of (A) g-C₃N₄NSs and (B) Ru–SiO₂ to different concentrations of RdRp gene (a: 0 nM, b ~ i: 10^{-6} to 10 nM). (C) The relationship between the ECL responses of g-C₃N₄NSs at 460 nm and Ru–SiO₂ at 620 nm with RdRp gene concentration. (D) lg(I$_{1(620nm)}$/I$_{2(460nm)}$) calibration plot for target RdRp gene detection.

detection limit was estimated to be 0.18 fmol L^{-1} (3σ/N). As can be seen from Table S2, the assay showed lower LOD compared to other assays for the detection of SARS-CoV-2 virus. In addition, the relative standard deviation (RSD) was calculated to be 2.5% by performing target (10 nM) for three times, indicating that the biosensor possesses well precision for assay and can be applied for quantitative detection of RdRp gene concentration.

3.8. Selectivity study of the ECL biosensor

The selectivity of this ECL biosensing system for detection of RdRp gene was verified, and the SARS-CoV RdRp gene, three-base mismatch DNA, and random DNA were used as interferers. Fig. S6 showed except for the SARS-CoV-2 RdRp gene, other DNAs have no obvious changes in the ratio of ECL signals. However, the mixed DNA group containing the SARS-CoV-2 RdRp gene showed ECL signal ratios close to that of the standard SARS-CoV-2 RdRp genome, these results indicate that the sensing system has good selectivity for SARS-CoV-2 RdRp gene detection.

3.9. Application of the method in analysis of actual samples

In order to test the effect of the ECL biosensor in actual detection, we mixed different concentrations of RdRp gene with healthy human throat swab samples, the recovery efficiency of different concentrations of the RdRp gene in actual human throat swab samples was detected by the standard addition method, the results are shown in Table S3. Here, the standard deviation was calculated with three sets of samples as a gradient, and the repeatability of the biosensor was carried out through detection of eight concentrations from 1 fM to 10 nM. The experimental recovery ranges from 92% to 102.1%, and the relative standard deviation is from 1.5% to 3.8%. This indicates that the designed ECL biosensor is applicable for human throat swab samples.

4. Conclusions

A novel ratiometric ECL biosensing platform based on RET mechanism between g-C$_3$N$_4$NSs and Ru–SiO$_2$ combined with 3D DNA walker amplification was prepared to detect RdRp gene, showing excellent advantages. Firstly, g-C$_3$N$_4$NSs and Ru–SiO$_2$ displayed stable and outstanding electrochemiluminescence properties at two distinguishable wavelengths, which can be used to design the ratiometric ECL biosensor. Secondly, the ECL emission peak of g-C$_3$N$_4$ NSs perfectly overlaps with the UV absorption peak of Ru–SiO$_2$, guaranteeing effective ECL RET for biosensor. Thirdly, the triple-helix capture DNA was stably and vertically immobilized on the surface of g-C$_3$N$_4$NSs, which much improved binding efficiency of DNA and detection sensitivity of biosensor. Fourthly, the target gene was amplified by 3D DNA walker and achieved ultrasensitive assay. Therefore, this work not only developed a unique ratio-type ECL strategy for clinical detection of SARS-gene, but also established a new biosensing technology using the promising carbon ECL nanomaterial.

CRediT authorship contribution statement

Tengyue Yin: Writing – original draft. **Yuhang Ye:** Data curation. **Wenshuai Dong:** Formal analysis. **Guifen Jie:** Writing – review & editing.

Declaration of competing interest

The authors declare that they have no known competing financial interests or personal relationships that could have appeared to influence the work reported in this paper.

Data availability

No data was used for the research described in the article.

Appendix A. Supplementary data

Supplementary data to this article can be found online at https://doi.org/10.1016/j.bios.2022.114580.

References

Agrawal, N., Saha, C., Kumar, C., Singh, R., Zhang, B., Jha, R., Kumar, S., 2020. IEEE Sensor. J. 20, 11372–11379.

Chang, C.C., Chen, C.P., Chen, C.Y., Lin, C.W., 2016. Chem. Commun. 52, 4167–4170.

Chen, Y., Sun, D., Du, L., Jiao, Y., Han, W., Tian, G., 2022. ACS Appl. Mater. Interfaces 14, 24425–24434.

Cheng, Y., Huang, Y., Lei, J., Zhang, L., Ju, H., 2014. Anal. Chem. 86, 5158–5163.

Dai, W., Dong, H., Guo, K., Zhang, X., 2018. Chem. Sci. 9, 1753–1759.

Dong, Y.-P., Wang, J., Peng, Y., Zhu, J.-J., 2016. J. Electroanal. Chem. 781, 109–113.

Engelmann, I., Alidjinou, E.K., Ogiez, J., Pagneux, Q., Miloudi, S., Benhalima, I., Ouafi, M., Sane, F., Hober, D., Roussel, A., Cambillau, C., Devos, D., Boukherroub, R., Szunerits, S., 2021. ACS Omega 6, 6528–6536.

Fan, Z., Yao, B., Ding, Y., Zhao, J., Xie, M., Zhang, K., 2021. Biosens. Bioelectron. 178, 113015.

Feng, C., Wang, Z., Chen, T., Chen, X., Mao, D., Zhao, J., Li, G.A., 2018. Anal. Chem. 90, 2810–2815.

Feng, Q.M., Shen, Y.Z., Li, M.X., Zhang, Z.L., Zhao, W., Xu, J.J., Chen, H.Y., 2016. Anal. Chem. 88, 937–944.

Gai, P., Gu, C., Li, H., Sun, X., Li, F., 2017. Anal. Chem. 89, 12293–12298.

Ge, J., Zhao, Y., Li, C., Jie, G., 2019. Anal. Chem. 91, 3546–3554.

Guo, W., Ding, H., Gu, C., Liu, Y., Jiang, X., Su, B., Shao, Y., 2018. J. Am. Chem. Soc. 140, 15904–15915.

Huang, Y., Lei, J., Cheng, Y., Ju, H., 2016. Biosens. Bioelectron. 77, 733–739.

Hyeon, J.E., Jeong, D.W., Ko, Y.J., Kim, S.W., Park, C., Han, S.O., 2018. Biosens. Bioelectron. 114, 1–9.

Jie, G., Li, C., Zhao, Y., Kuang, Q., Niu, S., 2019. ACS Appl. Nano Mater. 2, 4637–4645.

Li, M., Li, J., Sun, L., Zhang, X., Jin, W., 2012. Electrochim. Acta 80, 171–179.

Liang, R.P., Yu, L.D., Tong, Y.J., Wen, S.H., Cao, S.P., Qiu, J.D., 2018. Chem. Commun. 54, 14001–14004.

Liu, C., Zhou, Q., Li, Y., Garner, L.V., Watkins, S.P., Carter, L.J., Smoot, J., Gregg, A.C., Daniels, A.D., Jervey, S., Albaiu, D., 2020. ACS Cent. Sci. 6, 315–331.

Liu, L., Zhang, Y., Yuan, R., Wang, H., 2020. Anal. Chem. 92, 15112–15119.

Liu, Y., Wang, M., Nie, Y., Zhang, Q., Ma, Q., 2019. Anal. Chem. 91, 6250–6258.

Maar, R.R., Zhang, R., Stephens, D.G., Ding, Z., Gilroy, J.B., 2019. Angew Chem. Int. Ed. Engl. 58, 1052–1056.

Ma, H., Li, X., Yan, T., Li, Y., Liu, H., Zhang, Y., Wu, D., Du, B., Wei, Q., 2016. ACS Appl. Mater. Interfaces 8, 10121–10127.

Ma, J., Wang, W., Li, Y., Lu, Z., Tan, X., Han, H., 2021. Anal. Chem. 93, 2090–2096.

Majdoub, M., Anfar, Z., Amedlous, A., 2020. ACS Nano 14, 12390–12469.

Medetalibeyoğlu, H., 2021. Carbon Lett. 31, 1237–1248.

Muzyka, K., Saqib, M., Liu, Z., Zhang, W., Xu, G., 2017. Biosens. Bioelectron. 92, 241–258.

Ong, W.J., Tan, L.L., Ng, Y.H., Yong, S.T., Chai, S.P., 2016. Chem. Rev. 116, 7159–7329.

Pu, G., Zhang, D., Mao, X., Zhang, Z., Wang, H., Ning, X., Lu, X., 2018. Anal. Chem. 90, 5272–5279.

Qing, M., Xie, S., Cai, W., Tang, D., Tang, Y., Zhang, J., Yuan, R., 2018. Anal. Chem. 90, 11439–11445.

Shahdeo, D., Roberts, A., Archana, G.J., Shrikrishna, N.S., Mahari, S., Nagamani, K., Gandhi, S., 2022. Biosens. Bioelectron. 212, 114406.

Sun, P., Liu, B., You, Z., Zheng, Y., Wang, Z., 2022. ACS Appl. Nano Mater. 5, 3450–3457.

Tang, J., He, X., Lei, Y., Shi, H., Guo, Q., Liu, J., He, D., Yan, L., Wang, K., 2017. Chem. Commun. 53, 11889–11892.

Volokh, M., Peng, G., Barrio, J., Shalom, M., 2019. Angew Chem. Int. Ed. Engl. 58, 6138–6151.

Wang, Y., Zhang, Y., Sha, H., Xiong, X., Jia, N., 2019. ACS Appl. Mater. Interfaces 11, 36299–36306.

Wei, X., Zhu, M.J., Cheng, Z., Lee, M., Yan, H., Lu, C., Xu, J.J., 2019. Angew. Chem., Int. Ed. Engl. 58, 3162–3166.

Wu, P., Hou, X., Xu, J.J., Chen, H.Y., 2016. Nanoscale 8, 8427–8442.

Wu, T., Cao, Y., Yang, Y., Zhang, X., Wang, S., Xu, L.P., Zhang, X., 2019. Nanoscale 11, 11279–11284.

Xiong, H., Gao, J., Wang, Y., Chen, Z., Chen, M.M., Zhang, X., Wang, S., 2019. Analyst 144, 2550–2555.

Xu, X., Zhang, P., Zhang, R., Zhang, N., Jiang, W., 2019. Chem. Commun. 55, 6026–6029.

Yang, J., Wu, Y., Gan, C., Yuan, R., Xiang, Y., 2018. Biosens. Bioelectron. 117, 743–747.

Yang, X., Wei, Y., Wang, Z., Wang, J., Qi, H., Gao, Q., Zhang, C., 2022. Anal. Chem. 94, 2305–2312.

Ye, J., Zhu, L., Yan, M., Zhu, Q., Lu, Q., Huang, J., Cui, H., Yang, X., 2019. Anal. Chem. 91, 1524–1531.

Zhao, M., Bai, L., Cheng, W., Duan, X., Wu, H., Ding, S., 2019. Biosens. Bioelectron. 127, 126–134.

Zhou, C., Chen, Y., Shang, P., Chi, Y., 2016. Analyst 141, 3379–3388.

Zhou, Z., Zhang, Y., Shen, Y., Liu, S., Zhang, Y., 2018. Chem. Soc. Rev. 47, 2298–2321.

Zhong, X., Nayak, S., Guo, L., Raidas, S., Zhao, Y., Weiss, R., Andisik, M., Elango, C., Sumner, G., Irvin, S.C., Partridge, M.A., Yan, H., Qiu, H., Mao, Y., Torri, A., Li, N., 2021. Anal. Chem. 93, 12889–12898.

Zhu, S., Lin, X., Ran, P., Xia, Q., Yang, C., Ma, J., Fu, Y., 2017. Biosens. Bioelectron. 91, 436–440.

Zhu, Q., Mao, W., Zhang, C., Zhou, Y., Tang, Z., Yu, C., 2020. Anal. Chim. Acta 1140, 89–98.

Zou, R., Lin, Y., Lu, C., 2021. Anal. Chem. 93, 2678–2686.